Inorganic Chemistry

pubs.acs.org/IC Article

High-Frequency EPR Studies of New 2p−3d Complexes Based on a Triazolyl-Substituted Nitronyl Nitroxide Radical: The Role of Exchange Anisotropy in a Cu−Radical System

Mateus S. de Souza, Samira G. Reis, Danilo Stinghen, Lívia B. L. Escobar,* Rafael A. Allão Cassaro, Giordano Poneti, Carolina S. Bortolot, Jonathan Marbey, Stephen Hill,* and Maria G. F. Vaz*

Cite This: *Inorg. Chem.* 2022, 61, 12118−12128 Read Online

ACCESS | Metrics & More | Article Recommendations | Supporting Information

ABSTRACT: Using the 1-(*m*-tolyl)-1*H*-1,2,3-triazole-4-(4,4,5,5-tetramethylimidazoline-1-oxyl-3-oxide) (TlTrzNIT) radical and metal *β*-diketonate complexes [M(hfac)$_2$(H$_2$O)$_2$], where hfac is hexafluoroacetylacetonato, three new 2p−3d heterospin complexes were synthesized. Their structures were solved using single crystal X-ray diffraction data, and magnetic investigation was performed by DC and AC measurements and multifrequency EPR spectroscopy. Compounds **1** and **2** are isostructural complexes with molecular formula [M$_3$(TlTrzNIT)$_2$(hfac)$_6$] (M^{II} = Mn or Cu) while compound **3** is the mononuclear [Co(TlTrzNIT)(hfac)$_2$] complex. In all complexes, the radical acts as a bidentate ligand through the oxygen atom of the nitroxide moiety and the nitrogen atom from the triazole group. Furthermore, in compounds **1** and **2**, the TlTrzNIT is bridge-coordinated between two metal centers, leading to the formation of trinuclear complexes. The fitting of the static magnetic behavior reveals antiferromagnetic and ferromagnetic intramolecular interactions for complexes **1** and **2**, respectively. The EPR spectra of **1** are well described by an isolated ferrimagnetic $S = {}^{13}/_2$ ($= {}^5/_2 - {}^1/_2 + {}^5/_2 - {}^1/_2 + {}^5/_2$) ground state with a biaxial zero-field splitting (ZFS) interaction characterized, respectively, by 2nd order axial and rhombic parameters, *D* and *E*, such that *E*/*D* is close to the maximum of 0.33. Meanwhile, EPR spectra for **2** are explained in terms of a ferromagnetic model with weakly anisotropic Cu−radical exchange interactions, giving rise to an isolated $S = {}^5/_2$ ($= 5 \times {}^1/_2$) ground state with both an anisotropic *g* tensor and a weak ZFS interaction. Complex **2** represents one of only a few examples of Cu−radical moieties with measurable exchange anisotropy.

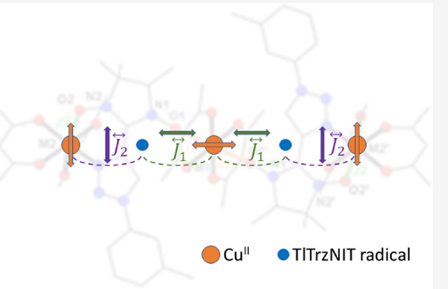

1. INTRODUCTION

The advent of single molecule magnets (SMMs) in the early 1990s[1] renewed the molecular magnetism field with great potential for technological advances.[2−6] Indeed, the application of molecule-based magnets to high-density data storage and data processing devices[7−9] remains one of the most enticing challenges in the field. The promise of such applications has, in turn, spurred great progress in understanding the mechanisms that govern magnetic relaxation.[10,11] Of particular interest to synthetic chemists are the strategies that may be employed for the preparation of molecules with a large energy barrier for reversal of magnetization and high blocking temperatures obtained mainly for mononuclear lanthanide-based complexes.[12−16] However, the magnetic relaxation in most of the lanthanide-based SMMs is accelerated due to the quantum tunneling of the magnetization (QTM), and no hysteresis loop or small coercive fields are often observed. On the other hand, a promising strategy to suppress QTM is to introduce strong intramolecular magnetic interactions involving anisotropic metal centers.[17,18]

Magnetic properties are governed by intramolecular magnetic interactions between paramagnetic centers in polynuclear species such as dimers, trimers, and so on. In most of the cases, the non-degenerate ground state of the ligand field term of interacting ions leads to magnetic interactions modeled using the Heisenberg-Dirac Hamiltonian. However, the description of magnetic interactions between paramagnetic metals with degenerate ground state ligand field terms is more complicated and requires a specific formalism.[19] In these cases, the magnetic interaction is anisotropic and related to the unquenched orbital angular momentum of the interacting ions. Strong anisotropic magnetic interactions can be a source of the overall magnetic anisotropy in polynuclear systems, leading to SMM behavior with an energy barrier for reversal of magnetization related to the strength of the exchange anisotropy[19−21] and also to the number of magnetic interacting centers.[22] This discovery can be considered a

Received: February 28, 2022
Published: July 25, 2022

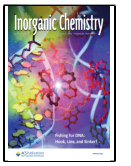

https://doi.org/10.1021/acs.inorgchem.2c00679
Inorg. Chem. 2022, 61, 12118−12128

strategy for designing SMMs with high energy barriers and high blocking temperatures.

Nitroxide and nitronyl nitroxide radicals are building blocks widely applied as ligands and can provide complexes with diverse nuclearities such as polynuclear aggregates or coordination polymers.[23−27] Since this radical can coordinate to metal ions, strong metal−radical magnetic exchange interactions can be obtained.[24,25,28] In addition to magnetometry studies of copper(II)−radical systems, spectroscopic investigations using EPR techniques, particularly at high fields,[29] provide exquisite sensitivity to magnetic interactions. Known examples include studies of breathing crystals that exhibit temperature-dependent exchange interactions due to changes in intramolecular spin distances as a function of temperature[30,31] as well as investigations of magnetic dimensionality in weakly coupled systems, even at room temperature.[32] In this contribution, we report the synthesis of homometallic 3d complexes coordinated by the nitronyl nitroxide radical 1-(*m*-tolyl)-1*H*-1,2,3-triazole-4-(4,4,5,5-tetramethylimidazoline-1-oxyl-3-oxide) (TlTrzNIT). Three compounds are described, two trinuclear species of manganese(II) (**1**) or copper(II) (**2**) and one mononuclear cobalt(II) (**3**), as well as their structure, static, and dynamic magnetic properties. Multifrequency high field electron paramagnetic resonance was used to study the magnetic anisotropy, unveiling a biaxial zero-field splitting (ZFS) for **1**, while the EPR spectra for **2** are explained in terms of a ferromagnetic model with anisotropic Cu−radical exchange interactions.

2. EXPERIMENTAL SECTION

2.1. General. All reagents and solvents were purchased from commercial sources and used without further purifications. [M(hfac)$_2$(H$_2$O)$_2$][33] (M^{II} = Mn, Cu or Co) and the radical TlTrzNIT (Chart 1)[34] were synthesized using previously reported methods.

Chart 1. TlTrzNIT Radical

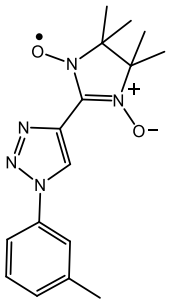

Infrared spectra were recorded using an Alpha-P Bruker spectrophotometer. Electronic absorption spectra were recorded in the 190−800 nm window using a Varian Cary 500 spectrophotometer, equipped with a Harrick Praying Mantis DRP diffuse reflection accessory. Measurements were performed in the solid-state, and all compounds were ground with MgO as a dilution medium. Elemental analyses were performed using a Perkin Elmer 2400 series II.

2.2. Syntheses of Compounds 1−3. All complexes were synthesized using the same procedure. 48 μmol of the [M(hfac)$_2$(H$_2$O)$_2$] (M^{II} = Mn, Cu or Co) was solubilized in 19 mL of boiling heptane, and the solution was kept under stirring and heat until the evaporation of half the initial volume. Then, a solution of 32 μmol of the TlTrzNIT radical dissolved in 1 mL of dichloromethane was added to the heptane solution. The resulting solution was kept at room temperature (for copper complex) or at 8 °C (manganese and cobalt complexes). Suitable single crystals for X-ray data collection were obtained as dark green blocks for **1** and **2** and as black blocks for **3**. The single crystals were formed more quickly for **1** while for **2** and **3**, they were obtained after 3−5 days. Yield: 31% (**1**); 60% (**2**); 66% (**3**). For **1** IR (ATR, cm^{-1}): 3156 (vw, ν (C−H)); 1641 (s, ν (C═O)); 1476 (m, δ (C−H)); 1351 (w, ν (N−O)); 1252, 1194, 1133, 1095, 1068 (s, ν (C−F)). Elemental analysis calculated for $C_{62}H_{46}F_{36}Mn_3N_{10}O_{16}$ (%) C = 35.58, H = 2.28, N = 6.88, found C = 35.75, H = 2.38, N = 6.83. For **2**: 3166 (vw, ν (C−H)); 1640 (s, ν (C═O)); 1466 (m, δ (C−H)); 1365 (w, ν (N−O)); 1252, 1215, 1193, 1136, 1082 (s, ν (C−F)). Calculated elemental analysis for $C_{62}H_{46}F_{36}Cu_3N_{10}O_{16}$ (%) C = 36.12, H = 2.25, N = 6.79; found C = 36.03, H = 2.40, N = 6.83. For **3**: 3118 (vw, ν (C−H)); 1641 (s, ν (C═O)); 1374 (w, ν (N−O)); 1255, 1195, 1132, 1095 (s, ν (C−F)). Calculated elemental analysis for $C_{26}H_{22}CoF_{12}N_5O_6$ (%) C = 39.66, H = 2.82, N = 8.89; found C = 39.83, H = 2.75, N = 8.83. UV−Vis (solid state, λ in nm) for **1** and **2**: 246 (broad shoulder), 307, 356 (π−π* for the TlTrzNIT ligand or the diketonate moieties),[35] 546, 591, 644 (ligand n−π* and MLCT transitions).[35] For **3**: 219 (broad shoulder), 260 (broad shoulder), 304, 351 (π−π* for the TlTrzNIT ligand or the diketonate moieties),[35] 537 (broad shoulder), 582, 645 (ligand n−π* and MLCT transitions).[35] The infrared and UV−visible spectra are shown in Figures S1−S3.

2.3. X-ray Diffraction. Single-crystal X-ray diffraction data were collected on a Bruker D8 Venture diffractometer with Mo Kα (λ = 0.71073 Å) radiation at 160 and 150 K for **1** and **2**, respectively and at room temperature for **3**. Data collection and cell refinement were performed with the Bruker Instrument ServiceV6.2.6 and the APEX3 programs, respectively.[36] Data reduction was performed using SAINT.[37] Empirical multiscan absorption correction using equivalent reflections was performed with the SADABS program.[38] All crystal structures were solved and refined using the SHELXS-97 and SHELXL-2018 programs, respectively.[39] The structures were drawn using the MERCURY software.[40] Large thermal displacement parameters were found for fluorine atoms due to thermal motion of disordered CF_3 groups. Methyl groups for **2** were also disordered. The occupancy of disordered atoms was freely refined, and constraints and restraints were applied to model the disorder. A summary of the crystal data, data collection, and refinement for compounds **1**−**3** is listed in Table 1. Selected bond lengths and bond angles are gathered in Table 2. The calculated coordination environment of all metal ions for compounds **1**−**3** is shown in Table S1. Powder X-ray diffraction data (PXRD) were collected on a Bruker D8 Advance equipped with a LynxEye detector at room temperature using Cu Kα radiation, with a step size of 0.02° and step time of 1 s. The experimental powder X-ray diffraction patterns agree with the simulated ones from the structures solved by single-crystal XRD data, indicating good crystal phase purity (Figures S4−S6 in the Supporting Information).

2.4. Magnetic Characterization. The DC magnetic measurements were performed in a Quantum Design MPMS-3 SQUID magnetometer under a DC external field of 1 kOe from 5 to 50 K and 10 kOe from 40 to 300 K. Alternating current magnetic susceptibility analyses were performed with a PPMS (physical properties measurement system) platform, also from Quantum Design, with oscillating field frequencies ranging from 10 to 10^4 Hz. All compounds were wrapped in polytetrafluoroethylene (PTFE) tape and pressed into a pellet before measurement. The data were corrected for the diamagnetic contribution of the sample[41] and holder.

2.5. EPR Spectroscopy. High-field, high-frequency electron paramagnetic resonance (HFEPR) measurements were carried out at the U.S. National High Magnetic Field Laboratory (NHMFL), in Tallahassee, Florida, on powder samples of compounds **1** and **2**. Powder spectra were recorded using magnetic field modulation at temperatures ranging from ca. 7 to 50 K on a home-built spectrometer. The instrument is a transmission-type device in which microwaves are propagated to the sample via cylindrical light pipes. A wide-band, low-noise, liquid helium cooled (4.2 K) InSb bolometer was employed for signal detection. After detection and preamplification, the signal is fed into a phase sensitive lock-in amplifier that is used to filter and process the signal intensity, *I*, that is in-phase with the field modulation frequency.[42] Consequently, the EPR spectra are

https://doi.org/10.1021/acs.inorgchem.2c00679
Inorg. Chem. 2022, 61, 12118−12128

Table 1. Summary of the Crystal Structure, Data Collection, and Refinement for 1−3

compound reference	1	2	3
chemical formula	$C_{62}H_{46}F_{36}Mn_3N_{10}O_{16}$	$C_{62}H_{46}F_{36}Cu_3N_{10}O_{16}$	$C_{26}H_{22}CoF_{12}N_5O_6$
formula mass/g mol^{-1}	2035.90	2061.71	787.41
crystal system	triclinic	triclinic	orthorhombic
space group	*P*-1	*P*-1	*Pbca*
radiation type	Mo Kα	Mo Kα	Mo Kα
temperature/K	160(2)	150(2)	298(2)
a/Å	9.2710(8)	9.1837(7)	13.3866(6)
b/Å	14.6256(15)	14.6025(11)	21.8646(8)
c/Å	16.0371(17)	16.2274(12)	23.2962(10)
α/°	96.397(5)	94.328(3)	90
β/°	101.121(4)	104.081(2)	90
γ/°	108.071(4)	107.526(2)	90
V/Å^3	1994.0(3)	1986.6(3)	6818.6(5)
Z	1	1	8
ρ/Mg m^{-3}	1.695	1.723	1.534
μ/mm^{-1}	0.620	0.949	0.614
reflections measured	63,563	59,759	73,540
independent reflections	7028	8167	5997
θ range/°	2.162−25.025	2.131−26.450	2.498−25.048
R_{int}	0.1300	0.0674	0.0602
R_1 ($I > 2\sigma(I)$)	0.0624	0.0515	0.0730
$wR(F^2)$ ($I > 2\sigma(I)$)	0.1261	0.1236	0.1630
R_1 (all data)	0.1007	0.0685	0.0980
$wR(F^2)$ (all data)	0.1448	0.1384	0.1784
goodness of fit on F^2	1.091	1.069	1.106
$\Delta\rho$max, $\Delta\rho$min (e·Å^{-3})	0.622, −0.539	0.956, −0.715	0.630, −0.523
CCDC deposition	2102486	2102487	2102488

Table 2. Selected Bond Lengths (Å) and Bond Angles (°) for Compounds 1−3

1		2		3	
		Bond lengths (Å)			
Mn1−O1	2.173(3)	Cu1−O1	2.396(2)	Co1−O2	2.063(3)
Mn1−O7	2.110(3)	Cu1−O7	1.940(2)	Co1−O3	2.056(4)
Mn1−O8	2.127(3)	Cu1−O8	1.941(2)	Co1−O4	2.072(3)
Mn2−O2	2.184(3)	Cu2−O2	2.345(3)	Co1−O5	2.048(4)
Mn2−O3	2.128(3)	Cu2−O3	1.952(2)	Co1−O6	2.061(3)
Mn2−O4	2.124(3)	Cu2−O4	1.950(2)	Co1−N3	2.108(4)
Mn2−O5	2.150(3)	Cu2−O5	2.271(3)		
Mn2−O6	2.153(3)	Cu2−O6	1.982(2)		
Mn2−N3	2.216(4)	Cu2−N3	1.993(3)		
		Bond angles (°)			
O1−Mn1−O7	93.21(11)	O1−Cu1−O7	94.82(9)	O2−Co1−O3	177.97(14)
O1−Mn1−O8	94.08(11)	O1−Cu1−O8	93.79(9)	O2−Co1−O4	92.98(12)
O7−Mn1−O8	85.12(13)	O7−Cu1−O8	93.03(9)	O2−Co1−O5	90.59(14)
O2−Mn2−O3	121.9(3)	O2−Cu2−O3	97.10(10)	O2−Co1−O6	91.99(13)
O2−Mn2−O6	87.34(12)	O2−Cu2−O6	85.49(10)	O2−Co1−N3	84.98(13)
O2−Mn2−O4	94.19(13)	O2−Cu2−O4	92.70(10)	O3−Co1−O4	87.72(14)
O2−Mn2−O5	166.75(12)	O2−Cu2−O5	170.11(9)	O3−Co1−O5	91.28(15)
O2−Mn2−N3	79.13(12)	O2−Cu2−N3	81.76(10)	O3−Co1−O6	87.26(14)
O3−Mn2−O4	82.73(12)	O3−Cu2−O4	91.55(10)	O3−Co1−N3	93.09(15)
O3−Mn2−O5	92.31(13)	O3−Cu2−O5	91.85(10)	O4−Co1−O5	92.59(14)
O3−Mn2−N3	90.56(12)	O3−Cu2−N3	88.90(10)	O4−Co1−N3	92.72(14)
O4−Mn2−O6	86.00(12)	O4−Cu2−O6	87.05(10)	O4−Co1−O6	174.80(14)
O4−Mn2−O5	93.05(13)	O4−Cu2−O5	91.25(10)	O5−Co1−O6	88.87(14)
N3−Mn2−O5	95.07(12)	N3−Cu2−O5	94.27(10)	O6−Co1−N3	86.20(14)

recorded in derivative mode, dI/dB, where B is the applied field strength. The microwaves are generated using a phase-locked source followed by a multiplier chain (Virginia Diodes Inc.), generating frequencies in the range from 50.1 to 407 GHz. A superconducting magnet (Oxford Instruments plc) capable of reaching a field of 17 T was employed. The pure powder samples were obtained by grinding a batch of single crystals, which were then constrained to prevent magnetic torquing at high fields.

https://doi.org/10.1021/acs.inorgchem.2c00679
Inorg. Chem. 2022, 61, 12118−12128

3. RESULTS AND DISCUSSION

3.1. Syntheses and Crystal Structures. The reaction between $[M(hfac)_2(H_2O)_2]$ and the TlTrzNIT radical leads to the formation of isostructural complexes $[M_3(TlTrzNIT)_2(hfac)_6]$ (M^{II} = Mn (**1**) or Cu (**2**)) and the complex $[Co(TlTrzNIT)(hfac)_2]$ (**3**) whose structures are represented in Figures 1 and 2, respectively.

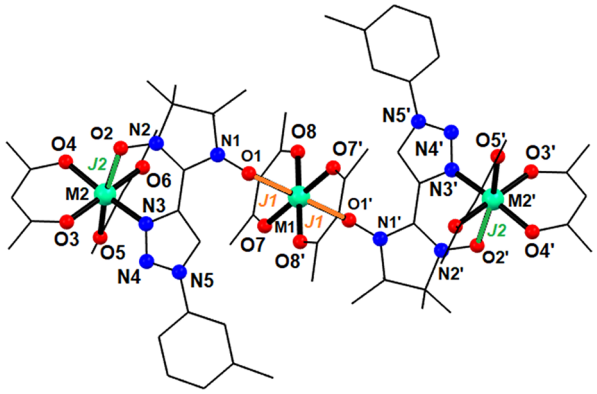

Figure 1. Representative crystal structure and magnetic interactions considered to fit magnetic susceptibility data of complexes **1** and **2**. Color code: black (carbon), red (oxygen), blue (nitrogen), green (copper(II) or manganese(II)). Hydrogen and fluorine atoms were omitted for clarity.

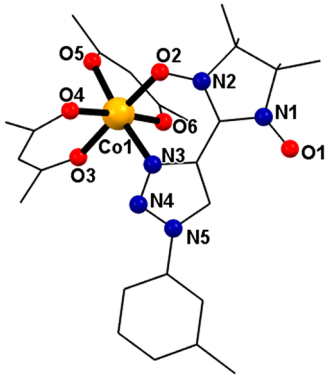

Figure 2. Structure of the asymmetric unit of complex **3**. Color code: black (carbon), red (oxygen), blue (nitrogen), orange (cobalt(II)). Hydrogen and fluorine atoms were omitted for clarity.

Compounds **1** and **2** crystallize in the triclinic *P*-1 space group and they are trinuclear complexes containing nitronyl nitroxide derivatives as ligands. Each metal ion is coordinated by two bidentate hfac ligands and one or two TlTrzNIT radicals. One of the metal centers, M1, lies on an inversion center, which determines the equivalence between the neighboring metal atoms (M2 and M2′), as well as the coordinated radical and hfac ligands. Each radical molecule is coordinated in a bridge mode connecting two metal centers (M1 and M2/M2′). In M2, the radical is coordinated in a bidentate mode through the oxygen atom from the nitroxide moiety (O2) and the nitrogen atom from the triazole ring (N3), while the second oxygen atom (O1) from two different radicals coordinates M1 in a monodentate fashion. For both complexes, the metal ions are found in a distorted octahedral geometry (Table S1) with elongated tetragonal distortion for **2** due to the Jahn−Teller effect with the oxygen atoms from the nitroxide group occupying the axial positions (see Table 2 for details). The Mn−O_{rad} bond lengths are different for Mn1 and Mn2, with values of 2.173(3) and 2.184(3) Å, respectively. The same occurs in the copper analogue, in which the Cu−O_{rad} bond lengths are 2.396(2) and 2.345(3) Å for Cu1 and Cu2, respectively, such that Cu1 is more axially elongated in comparison to Cu2. These bond lengths are in the range observed for other NIT radicals coordinated to the axial position of copper(II)[43,44] and are similar to other manganese(II)−NIT radicals reported in the literature.[45,46] In complex **1**, the N1−O1−Mn1 and N2−O2−Mn2 angles are 131.7(2) and 121.9(3)° while in complex **2**, the values found for the N1−O1−Cu1 and N2−O2−Cu2 angles are 136.6(2) and 117.6(2)°.

The intramolecular Mn1···Mn2 and Cu1···Cu2 distances are 6.7285(9) and 6.8170(6) Å, respectively. The shortest intermolecular distances between paramagnetic centers are 8.315(2) Å for Mn2···$Mn2^{i}$, 6.406(2) for Mn2···$O2^{i}$ (i = 1 − *x*, −*y*, 1 − *z*), 8.621(1) Å for Cu2···$Cu2^{ii}$ and 6.406(3) for Cu2···$O2^{ii}$ (ii = −*x*, −*y*, 1 − *z*), since the spin density of the NIT radicals is mainly located on the two nitrogen and two oxygen atoms from the nitroxide groups.[47] There are weak intermolecular interactions between hydrogen atoms from the methyl group and fluorine from the CF_3 group from adjacent molecules with a CH_2-H···F distance of 2.550 Å for **1** and 2.810 Å for **2**.

Compound **3** crystallizes in the orthorhombic *Pbca* space group. It is a mononuclear cobalt(II) complex in which the radical molecule acts as a bidentate ligand through the O2 and N3 atoms from the nitroxide and triazole moieties, and two bidentate hfac ligands complete the coordination environment. The metal center is found in a distorted octahedral geometry (Table S1). The Co−O_{rad} bond length is 2.063(3) Å and the N1−O2−Co1 angle is 120.5(2)°. Due to the bidentate mode of coordination of the radical ligand, the triazole ring cannot rotate freely. The dihedral angles (N2−C7−C8−N3) found between the NIT moieties and the triazole ring were 16.4(8)° for **1**, 18.2(5) for **2**, and 10.8(7) for **3**.

In the crystal packing of **3** (not shown), the units interact through F···H, N···H, and O···H contacts with distances in the range of 2.558−2.730 Å. The first one occurs between fluorine atoms from CF_3 groups and a hydrogen atom from CH_3 groups present in the NIT moiety. This interaction is also observed between the fluorine atoms and a hydrogen atom from the triazole ring. The triazole ring still interacts through the N4 atom (2.730 Å) with the hydrogen atom from a methyl group of the nitronyl nitroxide moiety. The last interaction is found between the oxygen atom from the hfac ligands and the hydrogen atom of the triazole ring. The shortest intermolecular distances between paramagnetic centers are 7.6509(7) and 6.084(3) Å for Co1···$Co1^{iii}$ and Co1···$O2^{iii}$ (iii = 0.5 + *x*, *y*, 0.5 − *z*), respectively.

3.2. Magnetic Study. The temperature dependence of the $\chi_M T$ products of compounds **1**, **2**, and **3** is reported in Figure 3. Compound **1** displays a $\chi_M T$ product of 14.17 emu.K/mol at 300 K, higher than the expected one for three uncoupled high-spin Mn(II) ions and two radicals (13.88 emu.K/mol), suggesting a magnetic coupling to be active among the paramagnetic ions and ligands at room temperature. Upon cooling, the $\chi_M T$ product increases monotonically, reaching a plateau at 23.60 emu.K/mol at 15 K. This value is close to that expected for an isotropic $S = {}^{13}/_{2}$ system (24.38 emu.K/mol), which suggests the presence of a ferrimagnetic structure

https://doi.org/10.1021/acs.inorgchem.2c00679
Inorg. Chem. 2022, 61, 12118−12128

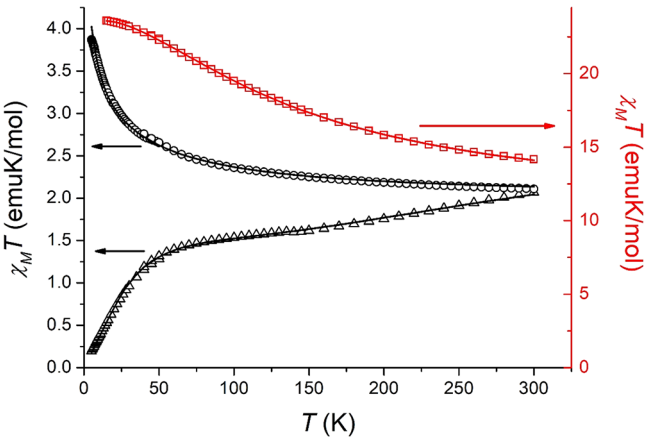

Figure 3. Temperature dependence of the $\chi_M T$ product of compounds **1** (squares), **2** (circles), and **3** (triangles). The lines are the results of the best fitting procedure with the model and parameters discussed in the text.

featuring a ground-state non-compensated spin arising from antiferromagnetic interactions between each Mn(II) ion and one or two radicals, i.e., $^5/_2 - {}^1/_2 + {}^5/_2 - {}^1/_2 + {}^5/_2 = {}^{13}/_2$. The field dependence of magnetization plot, measured at 2.0 K and reported in Figure S7, displays almost saturation with the value of 13.63 μ_B/mol at 7.,0 T, supporting this picture. In order to quantitatively describe the strength of the magnetic interactions present in **1**, a fit was performed using the PHI package.[48] Due to the centrosymmetric nature of the molecule, two different magnetic interactions were considered: J_1, which defines the exchange between the central Mn(II) ion and the surrounding radicals, and J_2, which describes the exchange between the lateral Mn(II) ions and the neighboring radicals (Figure 1). It must be stressed that the inclusion of additional interaction pathways was avoided to prevent overparametrization of the problem. Thus, in order to describe the isotropic exchange interactions present in the molecule, the Hamiltonian employed to fit the data was

$$\hat{H} = (1-\rho)\left[-2J_1\sum_{i=1}^{2}(\hat{S}_{M1}\cdot\hat{S}_{rad,i}) - 2J_2\sum_{i=1}^{2}(\hat{S}_{M2,i}\cdot\hat{S}_{rad,i}) + \sum_{i=1}^{5}\mu_B g_i\vec{B}\cdot\hat{S}_i\right] + \rho\mu_B g\vec{B}\cdot\hat{S}_{imp} \quad (1)$$

where the first two terms correspond to the magnetic interactions between the spins of the metal ions and radicals and the third defines the Zeeman interaction; μ_B is the Bohr magneton, $\vec{B}$ is the applied external field, and ρ and $\hat{S}_{imp}$ describe the molar fraction and spin of a mononuclear impurity ($S_{imp} = {}^5/_2$ for **1** and $^1/_2$ for **2**), respectively. The results of the best-fitting procedure of the $\chi_M T$ plot of **1** gave $J_1 = -268$ cm^{-1}, $J_2 = -71$ cm^{-1}, and a molar fraction of $g = 2.00$ magnetic impurity of 4%, with the Landé factors of the Mn(II) ions and of the organic radical being fixed to 2.00. Since there are shorter bond lengths for Mn1−O1 compared to Mn2−O2, a stronger intramolecular magnetic interaction is expected for the former due to shorter distances between paramagnetic centers. The obtained results confirm the strong antiferromagnetic interactions between the Mn(II) ions and the radicals. Previous studies of similar Mn-NIT radicals usually show moderate antiferromagnetic interactions (−77 cm^{-1},[49] and −76.8 cm^{-1},[50] with the same Hamiltonian used in this work). However, when coordinated by two NIT radicals, the antiferromagnetic interaction appears to be strengthened (−172 and −178 cm^{-1}).[51] Compound **1** represents a confirmation of this magneto-structural correlation.

The $\chi_M T$ product of compound **2** shows a room temperature value of 2.06 emu.K/mol, which slowly increases upon cooling to reach the value of 3.87 emu.K/mol at 2 K. Contrary to the case of **1**, this indicates the presence of ferromagnetic interactions in the molecular structure, leading to a total ground spin state of $S = {}^5/_2$ ($= 5 \times {}^1/_2$). The value of the spin of the ground state can be accessed also through the saturation value of the magnetization, measured at 2.0 K and reported in Figure S7, which saturates at 5.37 μ_B/mol. Using the Hamiltonian of eq 1, the following best-fitting parameters were obtained: $J_1 = +8.3$ cm^{-1}, $J_2 = +30$ cm^{-1}, and a molar fraction of paramagnetic impurity of 6% with the g values fixed from EPR (see below). As observed for **1**, the shorter Cu2−O2 bond length is expected to give stronger magnetic interaction. A ferromagnetic interaction is usually found for axially coordinated Cu(II)−NIT radicals.[52] It is worth mentioning that the kind of magnetic interaction in Cu(II)−NIT systems depends on which site of the coordination sphere is occupied by the oxygen atom from the nitroxide moiety. In general, most of the Cu(II)-radical examples reported in the literature show an elongated tetragonal distortion of the octahedral coordination environment. In this case, the oxygen atom from the radical can occupy the equatorial plane or the axial position. When it is located at the axial position, the Singly Occupied Molecular Orbital (SOMO) orbital from the NIT radical is orthogonal to the magnetic $d_{x^2-y^2}$ orbital of Cu(II), leading to a ferromagnetic interaction. In complex **2**, the radicals occupy the axial positions (longer bond lengths). An antiferromagnetic interaction is usually observed when the radical occupies at least one equatorial position.[25,53] On the other hand, for high-spin Mn(II) complexes, all five 3d orbitals have unpaired electrons. In this case, most of the 3d orbitals are not orthogonal to the radical SOMO leading to an antiferromagnetic interaction, as observed for complex **1**.[25]

Finally, compound **3** shows a $\chi_M T$ product of 2.06 emu.K/mol at 300 K, which almost linearly decreases to 1.62 emu.K/mol at 150 K. Below this temperature, the profile of the $\chi_M T$ product has the typical shape usually observed for octahedral high-spin Co(II) ions, decreasing to a value of 0.19 emu.K/mol at 5 K due to the unquenched angular orbital magnetism of the ion. The fact that the $\chi_M T$ product of **3** at room temperature is lower than the one expected for uncoupled high-spin Co(II) ion and an organic radical (2.7−3.2 emu.K/mol), as well as its decrease upon cooling, clearly indicates the presence of an antiferromagnetic interaction between the metal ion and the radical in **3**. A fit of the temperature dependence of the $\chi_M T$ and isothermal magnetizations plots has been carried out with the Hamiltonian (eq 2), and the results are reported in Figure 3, Figure S8, and Table S2:

$$\hat{H} = -2J\hat{S}_{Co}\cdot\hat{S}_{rad} + \sum_{i=x,y,z}\mu_B g_{Co,i}\vec{B}\cdot\hat{S}_{Co} + \mu_B g_{rad}\vec{B}\cdot\hat{S}_{rad} + D\hat{S}_{Co,z}^2 + E(\hat{S}_{Co,x}^2 - \hat{S}_{Co,y}^2) \quad (2)$$

The interaction between the cobalt(II) ion and the radical spins is indeed antiferromagnetic, taking the value −102 cm^{-1}, which is in the range for cobalt complexes bound to nitronyl nitroxide radicals,[54,55] while the cobalt(II) ion displays an in-

https://doi.org/10.1021/acs.inorgchem.2c00679
Inorg. Chem. 2022, 61, 12118−12128

plane magnetic anisotropy with low rhombicity (D = 14.5 cm^{-1}, E = 0.013 cm^{-1}). Inclusion of an anisotropic exchange interaction did not significantly improve the fit and was thus discarded to prevent overparametrization.

The dynamics of the magnetization of the three complexes did not show any out-of-phase signal without the application of a static magnetic field (Figure S9). In the case of **1**, no slow relaxing susceptibility is observed, even in the presence of an applied field in the 0−3000 Oe range. On the other hand, the onset of an out-of-phase signal displayed upon application of a field up to 3000 Oe for **2** and 3500 Oe for **3** does not show any peaks in the 10^2−10^4 Hz frequency range available in our investigation.

3.3. EPR Spectroscopy. In order to characterize the magnetic anisotropy associated with compounds **1** and **2**, high-field EPR spectra were collected on a series of powder samples. The frequency and temperature dependences of the EPR spectra and their accompanying simulations[56] are displayed in Figures 4 and 6.

In order to simulate the EPR spectra of compound **1**, a giant-spin approximation (GSA) was employed, which is justified when the coupled ground spin state is well separated from excited states, as would be expected on the basis of the large exchange parameters obtained from the magnetic fits.[57] We thus employed the following spin Hamiltonian to describe the S = $^{13}/_2$ ground state of **1**:

$$\hat{H} = \mu_B g \vec{B}\cdot\hat{S} + D\hat{S}_z^2 + E(\hat{S}_x^2 - \hat{S}_y^2) \quad (3)$$

The first term represents the Zeeman interaction, parameterized by an isotropic g factor (*vide infra*), while the last two terms, respectively, describe the second-order axial and rhombic zero-field splitting (ZFS) interactions, the strengths of which are given by the ZFS parameters, D and E. All simulations were performed using the program EasySpin.[56]

Figure 4a plots the experimental spectra and corresponding simulations for **1** as a function of the shift in magnetic field from the central transition, which also happens to be very close to the g = 2.00 position. Shifts away from the central position, B_c, are due to magnetic anisotropy. The key point to note is that the three strongest features, corresponding to the x, y, and z turning points of the powder spectra,[58] do not vary with field/frequency. Therefore, the magnetic anisotropy of **1** is dominated by a field-independent or ZFS interaction characterized by D and E; the field-dependent g anisotropy should therefore be weak. The other thing to note is that the low- and high-field shifts are almost identical (−0.456 and 0.486, respectively). This implies extreme biaxiality such that $E/D \approx 1/3$ (for axial cases, these shifts adopt a 2:1 ratio).[59,60] In the exact biaxial limit, the sign of D is undetermined, i.e., the system may be described as having either an easy axis (D < 0) with a highly anisotropic hard-plane, or a hard axis (D > 0) with a highly anisotropic easy plane. The best simulations are obtained with D = +0.037 cm^{-1} and E = +0.012 cm^{-1} (E/D = 0.324) with an isotropic g = 2.00. In order to replicate the fact that fine-structure peaks are clearly seen only on the low-field side of the spectra (i.e., $B - B_c$ < 0 T), a small strain in the rhombic parameter was included in the simulations, which broadens the fine structures in the xy region of the spectra so that they are not clearly resolved.[61] Here, the strain is defined by considering a small distribution, σ_E = 3 × 10^{-3} cm^{-1} centered at E = +0.012 cm^{-1}. The resultant simulations are thus formed from a convolution of multiple spectra sampled over the distribution in E, each having an isotropic peak-to-peak linewidth of 1.9 mT.

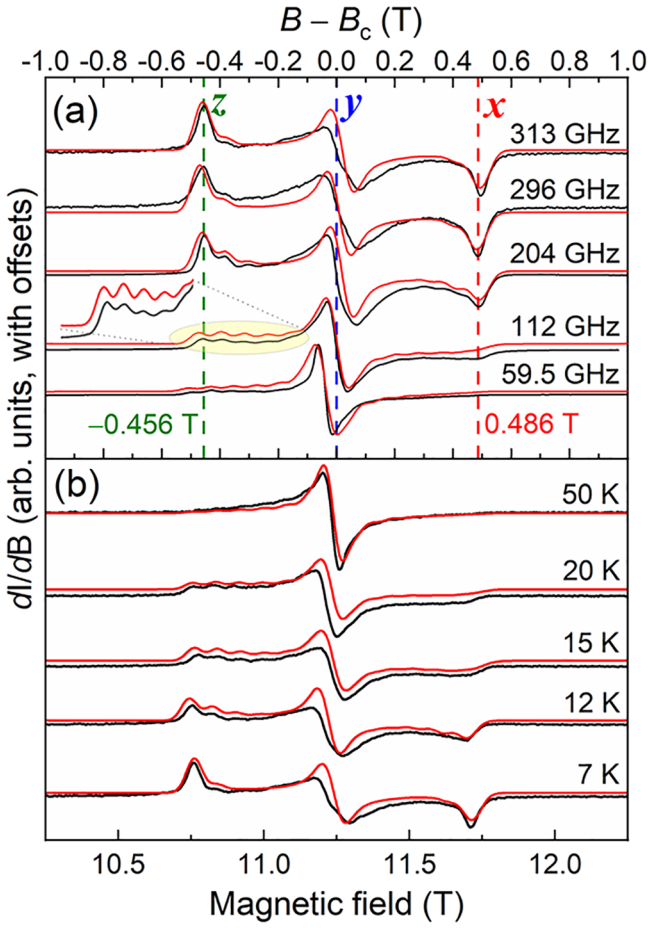

Figure 4. Frequency dependence of the experimental (black) and simulated (red) powder EPR spectra recorded at 7 K for **1**, plotted as a function of the deviation, $B - B_c$, from the center field, $B_c \approx hf/g\mu_B$, of each spectrum; h is Planck's constant, f is the measurement frequency, and g = 2. In this way, the spectra line up and one sees that the anisotropy is field/frequency-independent. A portion of the 112 GHz spectrum (highlighted in yellow) has been expanded vertically to show the agreement between the experimental and simulated fine structures, providing confirmation for the S = $^{13}/_2$ ground state. The vertical red, blue, and green dashed lines, respectively, mark the x, y, and z turning points of the spectra. (b) Temperature dependence of the experimental (black) and simulated (red) powder EPR spectra recorded at 313 GHz for **1**.

A portion of the 112 GHz spectrum in Figure 4a has been expanded to show the good alignment of the experimental and simulated fine-structure peak positions associated with the low field (z-) component of the powder pattern. This provides independent confirmation for the S = $^{13}/_2$ ground state, which results in $^1/_2(2S - 1)$ = 6 fine-structure peaks to the left of the g = 2.00 position. It is not possible to achieve such agreement for the ferromagnetic case (S = $^{17}/_2$), which would require two extra peaks spanning this 0.456 T range. Meanwhile, Figure 4b presents high-field (313 GHz) temperature-dependent measurements. As can be seen, the simulations match well over the entire range. At the lowest temperature, the spectrum is dominated by a single ground-state transition for each of the x, y, and z turning points of the powder pattern, i.e., a peak (dip) at the low (high) field extreme, and a derivative feature at the center. At the highest temperatures, all states of the S = $^{13}/_2$

https://doi.org/10.1021/acs.inorgchem.2c00679
Inorg. Chem. 2022, 61, 12118−12128

manifold are populated, and the spectrum is dominated by the $m_S = -^1/_2$ to $+^1/_2$ transitions that have the strongest matrix element[62] and also tend to be stronger because they are not affected by D strain.[63,64]

Similar EPR measurements were carried out on a powder of complex **2**. Frequency-dependent spectra, plotted in the same way as the data for **1** in Figure 4a, are displayed in Figure 6a. One immediately sees very obvious differences between the two compounds. In particular, **2** exhibits a very strong field-dependent magnetic anisotropy, in contrast to **1**. Because complex **2** comprises five $s = ^1/_2$ entities, for which there can be no associated ZFS (as dictated by Kramers' theorem), it is natural to assume that the splitting seen in the high-field spectrum is due entirely to g anisotropy [an effect not included in eq 2]. Indeed, the $3d^9$ electronic configuration associated with the Cu(II) ion is orbitally degenerate. A Jahn–Teller effect quenches the 1st order orbital contribution to the g-tensor anisotropy. However, a significant axiality typically remains, with as much as a 20% variation between principal components. We therefore rescaled the spectra and plotted them as a function of g value in Figure 6b. Remarkably, the spectra still do not perfectly line up, suggesting an additional source of anisotropy that is field-independent. Naturally, it is possible to simulate such spectra using a modified version of the GSA given in eq 2, which accounts for an anisotropic g tensor. Upon doing so, one obtains the following spin Hamiltonian parameters for **2**: $S = ^5/_2$, $D = -0.067$ cm^{-1}, $E = -0.014$ cm^{-1}, and $[g_x\ g_y\ g_z] = [2.04\ 2.07\ 2.17]$. However, the question arises as to the meaning of the associated D and E parameters since the only possible source of ZFS for a system of five $s = ^1/_2$ Kramers ions involves the spin–spin or exchange coupling Hamiltonian.[65,66] Of course, one possible source of such anisotropy would be the dipolar interaction between the spins. However, we can rule this out based on several observations that we discuss further below. We thus modified the multi-spin of eq 1 to include non-Heisenberg exchange interactions between the Cu(II) ions and radicals (Figure 5):[67]

$$\hat{H} = \mu_B \sum_{i=1}^{5} \vec{B}\cdot\vec{R}_i\cdot\vec{\tilde{g}}_i\cdot\vec{R}_i^{\,T}\cdot\hat{S}_i - 2\sum_{i=1}^{4} \hat{S}_i\cdot\vec{R}_{ij}\cdot\vec{\tilde{J}}_{ij}\cdot\vec{R}_{ij}^{\,T}\cdot\hat{S}_j \qquad (4)$$

Figure 5. Simplified schematic of the multi-spin Hamiltonian described by eq 4. Here, the orange double arrows denote the alignments of the principal (z-) axes of the g tensors associated with the Cu^{II} ions; the g tensors of the radicals are assumed to be isotropic. Meanwhile, the alignments of the principal (z-) axes of the two exchange tensors, $\vec{J}_1$ and $\vec{J}_2$, are represented by the green and purple double arrows, respectively.

The index i denotes the individual spins, whereas the interaction along the bonds between one site and the next must be described by two indices, i and $j = i + 1$. Indices $i = 1$, 3, and 5 correspond to Cu(II); $i = 1$ and 5 are the outermost sites (Cu2 and Cu2′), while $i = 3$ is the central one (Cu1). Meanwhile $i = 2$ and 4 correspond to the radicals. The main difference between eqs 1 and 4 is that the $\vec{\tilde{g}}_i$ and $\vec{\tilde{J}}_{ij}$ are now diagonal tensors. The rotation matrices, $\vec{R}_i$ and $\vec{R}_{ij}$, reflect the fact that these tensors need not be parallel on the different sites and, in fact, this turns out to be essential in achieving overall agreement between the experiments and spectral simulations.

Unfortunately, eq 4 has far too many parameters to constrain on the basis of the relatively simple spectra in Figure 6. Therefore, our aim here is to obtain simulations that capture

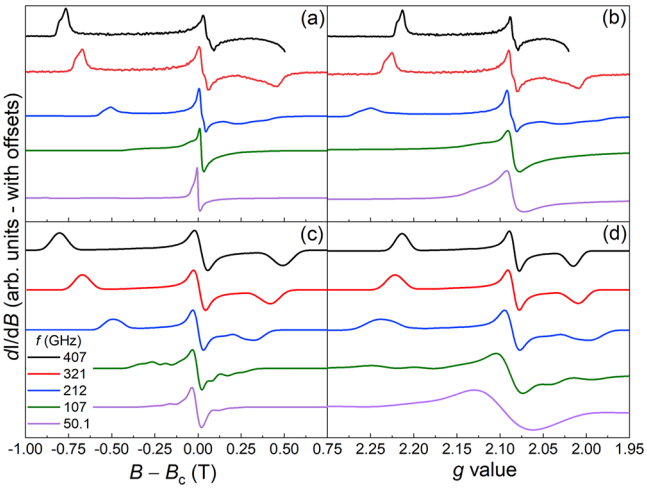

Figure 6. Frequency dependence of powder EPR spectra for **2** recorded at 7 K, plotted (a) as a function of the deviation, $B - B_c$, from the central peak position, B_c, and (b) as a function of g value by rescaling the abscissa according to $g = hf/\mu_B B$, where f is the measurement frequency [see legend in panel (c)]. The corresponding simulations according to eq 4 are displayed in panels (c) and (d), respectively; the parameters employed in the simulations are given in the main text.

the key features of the experimental spectra, thus demonstrating the importance of exchange anisotropy; note that, without this source of anisotropy, it would not be possible to simulate the spectra. However, the employed parameterization cannot be taken as exact because (i) the model has so much freedom that one may assume many parameter sets would give similar agreement and (ii) we must make several simplifying assumptions as a starting point for the simulations. To begin with, we assume that the g tensors associated with the radicals ($i = 2$, 4) are isotropic with diagonal components equal to 2.00. We then assume that the g tensors associated with the Cu(II) sites are axial such that $g_i^x = g_i^y < g_i^z (i = 1, 3, 5)$, which is fairly typical for Jahn–Teller elongated octahedral Cu(II) ions, for which the values range from about 2.05 to 2.50;[68] we also assume $\vec{\tilde{g}}_1 = \vec{\tilde{g}}_5$ due to the inversion symmetry. Based on the structural data in Table 2, we see that the Jahn–Teller axes on the outer and central Cu(II) ions (along O2–O5 and O1–O1′, respectively, see Figure 1) are significantly misaligned by about 57°. Therefore, for simplicity, we performed a 90° rotation of the g tensor of the central Cu(II) ($i = 3$).

Exchange anisotropy is not unexpected for Cu(II) due to its near orbital degeneracy.[66] Given that there is a direct correspondence with the spin-orbit physics responsible for both the $\vec{\tilde{g}}$ and $\vec{\tilde{J}}$ anisotropy,[69] we also enforced axiality onto the $\vec{\tilde{J}}$ tensors such that $J_{ij}^x = J_{ij}^y < J_{ij}^z$; we also assumed that $\vec{\tilde{J}}_{12} = \vec{\tilde{J}}_{45}$ and $\vec{\tilde{J}}_{23} = \vec{\tilde{J}}_{34}$, again due to inversion symmetry. We then rotated the inner J tensors by the same 90° matrix as the central g tensor, acknowledging the fact that any exchange anisotropy along those bonds reflects the spin-orbit coupling on the central Cu(II) ion. Finally, we set the average values of the inner and outer J tensor components to the ferromagnetic

https://doi.org/10.1021/acs.inorgchem.2c00679
Inorg. Chem. 2022, 61, 12118–12128

values deduced from the magnetic fits. Importantly, the magnitude of the exchange does not significantly influence the EPR simulations, provided $|\tilde{J}| > E_Z$, where E_Z ($=g\mu_B B$) characterizes the Zeeman energy. Only the exchange anisotropy matters, i.e., that J_{ij}^x, $J_{ij}^y \neq J_{ij}^z$. Therefore, we set $J_{ij}^x = J_{ij}^y = J_{ij}$ and $J_{ij}^z = J_{ij} + \delta_{ij}$. Moreover, in order to maintain consistency with the magnetic fits, we set $J_{12} = J_{45} = J_2$ (and $\delta_{12} = \delta_{45} = \delta_2$) and $J_{23} = J_{34} = J_1$ (and $\delta_{23} = \delta_{34} = \delta_1$). As an aside, the deduced exchange anisotropy is weak (of order 1−2% of the overall exchange, *vide infra*). Consequently, it has no discernible effect on the magnetic fit given in Figure 3. In other words, the anisotropic EPR parameterization is fully compatible with the magnetic data. Indeed, the two measurements complement each other: the magnetic fits constrain the isotropic exchange and are insensitive to the weak exchange anisotropy; meanwhile, the EPR simulations are sensitive only to the exchange anisotropy.

As can be seen from the simulations in Figure 6c,d [corresponding to the experimental spectra in Figure 6a,b], the model described above is able to achieve good overall agreement in terms of the main trends seen in the spectra. The employed parameters are as follows: $g_x = g_y = 2.08$ and $g_z = 2.48$ on the outer Cu ions (Cu2 and Cu2′) while $g_x = g_y = 2.05$ and $g_z = 2.30$ on the inner ion (Cu1); $J_1 = 8.00$ cm^{-1} and $J_2 = 30.0$ cm^{-1}, with $\delta_1 = 0.134$ cm^{-1} ($\approx 1.7\%$ of J_1) and $\delta_2 = 0.267$ cm^{-1} ($\approx 0.9\%$ of J_2). As one can see, the anisotropy energy scale is rather small in comparison to the Zeeman energy scale, particularly at the highest fields where $E_Z \approx 14$ cm^{-1}, and the anisotropy in the Zeeman interaction is about 10% of this number, i.e., ∼1.5 cm^{-1}. Therefore, *g*-tensor anisotropy dominates the trends, but the exchange anisotropy also causes measurable shifts in the spectral peak positions. The strategy for obtaining good simulations therefore first involved reproducing the positions of the three peaks on the basis of the *g* tensors. For these to be parallel, it would be impossible to reproduce the almost even spacing of the three main peaks in the spectra, which again correspond to the *x*, *y*, and *z* turning points of the powder pattern. In other words, it is the 90° rotation of the *g* tensor of the central Cu(II) that gives rise to a biaxial spectrum, as opposed to an axial one. Exchange anisotropies were then introduced in order to reproduce the shifts observed in Figure 6b. Finally, further adjustments were made to all parameters in order to obtain the best overall agreement.

As already noted, the ferromagnetic coupling gives rise to a spin $S = {}^5/_2$ ground state for **2**. One might therefore expect 2*S* fine structures associated with each component of the powder spectrum, as was the case for **1**; indeed, simulations with significantly reduced linewidths do reveal that these fine structure peaks clustered around the three main components of the spectrum. However, because the exchange anisotropy is weak, they are unresolved in the experiments, i.e., they are buried within the linewidths associated with the three *g*-tensor components. The simulations therefore considered strains in the *g* tensors (0.01 in every component for $i = 1, 3, 5$) and in δ_{ij} (50% FWHM), as well as an intrinsic 40 mT peak-to-peak linewidth. Although these strains are rather significant and not easy to reconcile based on structural considerations, the overall anisotropy energy scale is small, meaning that it must compete with other weak energy scales, e.g., due to intermolecular coupling (both dipolar and exchange) and unresolved hyperfine interactions, which can be quite significant for Cu(II).[66] For this reason, one should not expect perfect agreement between the simulations and experiments, particularly with regards to linewidths and the observation of some fine structures in the low-field spectra. However, the simulations do capture the overarching trends in the data, and the employed model is based on plausible physics. Our aim here is not to claim a definitive parameterization based on eq 4. Nevertheless, we believe it to be the correct model in this situation.

Returning to the issue of spin−spin dipolar interactions, we first note that one would expect more-or-less colinear dipolar coupling tensors due to the linear form of the molecule. However, as noted above, satisfactory spectral simulations are obtained only when assuming non-colinear exchange coupling tensors that follow the dispositions of the Jahn−Teller distortions on the Cu(II) ions. This strongly suggests that the source of the spin−spin coupling anisotropy is the same as that of the *g*-tensor anisotropy, which originates from the spin-orbit coupling on the Cu(II) sites, thus providing strong support to our assertion that this is due to exchange anisotropy.[66,68] Moreover, the exchange anisotropy energy scale determined from the simulations, $2\delta_{ij}S_iS_j \approx 0.07 - 0.13$ cm^{-1}, comfortably exceeds the dipolar anisotropy estimated on the basis of a point-dipole approximation (an average of ≈0.035 cm^{-1} for the Cu−radical interaction, assuming equal spacings between the five spins).

Previous works have shown that compounds possessing exchange anisotropy might provide an alternative route to obtaining highly anisotropic molecular nanomagnets instead of the use of the single-ion anisotropy.[22,70] In their analysis of the $[Mn^{III}Cu^{II}Cl(5\text{-Brsap})_2(MeOH)]$ complex, Singh and Rajaraman have illustrated that magnetic anisotropy can be a crucial parameter to determine the sign and strength of the global anisotropy.[71] The use of heavier metal ions such as Re(IV) is a promising strategy to obtain systems with pronounced anisotropic exchange since its complexes have diffuse and high-energy 5d orbitals favoring large exchange parameters with associated strong spin−orbit interactions (∼2000 cm^{-1} or more).[22] In 2010, Long and coworkers described the importance of the structural parameters in the magnitude and sign of the anisotropic exchange in the chain containing the Re(IV)−CN−Cu(II) moiety. The authors demonstrated experimentally and theoretically that the zigzag arrangement of the local tensors of the magnetic anisotropy around the Re(IV) ions dramatically reduces the effective magnetic anisotropy of the chain, thus explaining the absence of slow relaxation, despite the strong one-dimensional exchange.[72]

As discussed above, in complex **2**, we were able to deduce the exchange anisotropy because the Cu(II) ion is close to being orbitally degenerate. Even if no ZFS is present (because it is $s = {}^1/_2$), it has a fairly anisotropic *g* tensor, giving rise to a spin-orbit contribution to the exchange. In spite of the fact that the effects of anisotropic exchange are usually weak and hard to observe, we were able to detect them here because the exchange is strong. Interestingly, to the best of our knowledge, this is one of only a few examples of anisotropic exchange involving the Cu−radical moiety. A notable compound possessing a similar exchange interaction is given by a Cu(II) and an ortho-semiquinone radical,[73] which exhibits a triplet $S = 1$ ground state with an effective ZFS parameterized by $D = -1.09$ cm^{-1}. In this particular case, a simple point dipole interaction between the radical and the Cu(II) site was also not sufficient to explain the relatively large ZFS, which also pointed to the existence of anisotropic exchange.

https://doi.org/10.1021/acs.inorgchem.2c00679
Inorg. Chem. 2022, 61, 12118−12128

Finally, for complex **3**, the absence of any clear signal in the high-field EPR spectra suggests a large ZFS interaction.

4. CONCLUSIONS

Three new 2p−3d heterospin complexes were successfully synthesized employing the TlTrzNIT stable free radical as a ligand and $[M(hfac)_2(H_2O)_2]$ building blocks. All of the complexes were characterized via structural and spectroscopic methods, and their magnetic properties were investigated under a DC external magnetic field. The fits of the magnetic data reveal different types of magnetic interactions for each complex that are antiferromagnetic (complex **1**) and ferromagnetic (complex **2**). Detailed HFEPR analysis revealed an extreme magnetic biaxiality in complex **1** and confirmed the $S = {}^{13}/_{2}$ ground state, corroborating the magnetic susceptibility study. The *g* anisotropy added to the strong magnetic coupling between the Cu(II) ions and the radicals resulted in an exchange anisotropy present in complex **2**, a finding only made possible via the use of the multifrequency HFEPR. This is one of only a few examples of anisotropic exchange involving the Cu−radical moiety. The results obtained for this derivative may represent an alternative way to synthesize anisotropic molecular nanomagnets, with potential for development of improved single-molecule and single-chain magnets.

■ ASSOCIATED CONTENT

Supporting Information

The Supporting Information is available free of charge at https://pubs.acs.org/doi/10.1021/acs.inorgchem.2c00679.

IR and UV−Visible spectra, PXRD, and additional magnetic data (PDF)

Accession Codes

CCDC 2102486−2102488 contain the supplementary crystallographic data for this paper. These data can be obtained free of charge via www.ccdc.cam.ac.uk/data_request/cif, or by emailing data_request@ccdc.cam.ac.uk, or by contacting The Cambridge Crystallographic Data Centre, 12 Union Road, Cambridge CB2 1EZ, UK; fax: +44 1223 336033.

■ AUTHOR INFORMATION

Corresponding Authors

Lívia B. L. Escobar − *Instituto de Física, Universidade Federal Fluminense, Niterói 24210-346, Brazil; NHMFL, Florida State University, Tallahassee, Florida 32310, United States; Departamento de Química, Pontifícia Universidade Católica, Rio de Janeiro, RJ 22453-900, Brazil;* orcid.org/0000-0001-8899-0261; Email: liviablescobar@puc-rio.br

Stephen Hill − *NHMFL, Florida State University, Tallahassee, Florida 32310, United States; Department of Physics, Florida State University, Tallahassee, Florida 32306, United States;* orcid.org/0000-0001-6742-3620; Email: shill@magnet.fsu.edu

Maria G. F. Vaz − *Instituto de Química, Universidade Federal Fluminense, Niterói 24020-150, Brazil;* orcid.org/0000-0001-9855-5909; Email: mariavaz@id.uff.br

Authors

Mateus S. de Souza − *Instituto de Química, Universidade Federal Fluminense, Niterói 24020-150, Brazil*

Samira G. Reis − *Instituto de Química, Universidade Federal Fluminense, Niterói 24020-150, Brazil*

Danilo Stinghen − *Instituto de Química, Universidade Federal Fluminense, Niterói 24020-150, Brazil*

Rafael A. Allão Cassaro − *Instituto de Química, Universidade Federal do Rio de Janeiro, Rio de Janeiro 21941-909, Brazil;* orcid.org/0000-0002-0789-2561

Giordano Poneti − *Instituto de Química, Universidade Federal do Rio de Janeiro, Rio de Janeiro 21941-909, Brazil;* orcid.org/0000-0002-1712-4611

Carolina S. Bortolot − *Instituto de Química, Universidade Federal Fluminense, Niterói 24020-150, Brazil*

Jonathan Marbey − *NHMFL, Florida State University, Tallahassee, Florida 32310, United States; Department of Physics, Florida State University, Tallahassee, Florida 32306, United States*

Complete contact information is available at: https://pubs.acs.org/10.1021/acs.inorgchem.2c00679

Notes

The authors declare no competing financial interest.

■ ACKNOWLEDGMENTS

The authors thank FAPERJ and CNPq Brazilian agencies for the financial supports. This study was financed in part by the Coordenação de Aperfeiçoamento de Pessoal de Nível Superior-Brasil (CAPES) Finance Code 001. G.P. gratefully acknowledges FAPERJ for financial support through grants E-26/202.912/2019, SEI-260003/001167/2020, and E-26/010.000978/2019. We acknowledge the UFSCAR_QD_MPMS3 supported by FAPESP 09/54082-2 for the magnetic measurements, LDRX-UFF and LAME-UFF for use of the laboratory's facilities. SH acknowledges the support of the US National Science Foundation (NSF grant # DMR-2004732). Work performed at the NHMFL is supported by the NSF (under DMR-1644779) and the State of Florida.

■ REFERENCES

(1) Sessoli, R.; Gatteschi, D.; Caneschi, A.; Novak, M. A. Magnetic bistability in a metal-ion cluster. *Nature* **1993**, *365*, 141−143.

(2) Bagai, R.; Christou, G. The Drosophila of single-molecule magnetism: $[Mn_{12}O_{12}(OCR)_{16}(H_2O)_4]$. *Chem. Soc. Rev.* **2009**, *38*, 1011−1026.

(3) Rechkemmer, Y.; Breitgoff, F. D.; van der Meer, M.; Atanasov, M.; Hakl, M.; Orlita, M.; Neugebauer, P.; Neese, F.; Sarkar, B.; van Slageren, J. A four-coordinate cobalt(II) single-ion magnet with coercivity and a very high energy barrier. *Nat. Commun.* **2016**, *7*, 10467.

(4) Gomez-Coca, S.; Cremades, E.; Aliaga-Alcalde, N.; Ruiz, E. Mononuclear single-molecule magnets: tailoring the magnetic anisotropy of first-row transition-metal complexes. *J. Am. Chem. Soc.* **2013**, *135*, 7010−7018.

(5) Neese, F.; Pantazis, D. A. What is not required to make a single molecule magnet. *Faraday Discuss.* **2011**, *148*, 229−238.

(6) Serrano, G.; Poggini, L.; Briganti, M.; Sorrentino, A. L.; Cucinotta, G.; Malavolti, L.; Cortigiani, B.; Otero, E.; Sainctavit, P.; Loth, S.; Parenti, F.; Barra, A.-L.; Vindigni, A.; Cornia, A.; Totti, F.; Mannini, M.; Sessoli, R. Quantum dynamics of a single molecule magnet on superconducting Pb(111). *Nat. Mat.* **2020**, *19*, 546−551.

(7) Wernsdorfer, W.; Ruben, M. Synthetic Hilbert Space Engineering of Molecular Qudits: Isotopologue Chemistry. *Adv. Mat.* **2019**, *31*, 1806687/1−1806687/11.

(8) Gaita-Ariño, A.; Luis, F.; Hill, S.; Coronado, E. Molecular spins for quantum computation. *Nat. Chem.* **2019**, *11*, 301−309.

(9) Fittipaldi, M.; Cini, A.; Annino, G.; Vindigni, A.; Caneschi, A.; Sessoli, R. Electric field modulation of magnetic exchange in molecular helices. *Nat. Mater.* **2019**, *18*, 329−334.

(10) Lunghi, A.; Totti, F.; Sessoli, R.; Sanvito, S. The role of anharmonic phonons in under-barrier spin relaxation of single molecule magnets. *Nat. Commun.* **2017**, *8*, 14620.
(11) Briganti, M.; Santanni, F.; Tesi, L.; Totti, F.; Sessoli, R.; Lunghi, A. A Complete Ab Initio View of Orbach and Raman Spin−Lattice Relaxation in a Dysprosium Coordination Compound. *J. Am. Chem. Soc.* **2021**, *143*, 13633−13645.
(12) Goodwin, C. A. P.; Ortu, F.; Reta, D.; Chilton, N. F.; Mills, D. P. Molecular magnetic hysteresis at 60 kelvin in dysprosocenium. *Nature* **2017**, *548*, 439−442.
(13) Guo, F. S.; Day, B. M.; Chen, Y. C.; Tong, M. L.; Mansikkamäki, A.; Layfield, R. A. A Dysprosium Metallocene Single-Molecule Magnet Functioning at the Axial Limit. *Angew. Chem., Int. Ed.* **2017**, *56*, 11445−11449.
(14) Guo, F. S.; Day, B. M.; Chen, Y. C.; Tong, M. L.; Mansikkamäki, A.; Layfield, R. A. Magnetic hysteresis up to 80 kelvin in a dysprosium metallocene single-molecule magnet. *Science* **2018**, *362*, 1400−1403.
(15) Liu, J. L.; Chen, Y. C.; Tong, M. L. Symmetry strategies for high performance lanthanide-based single-molecule magnets. *Chem. Soc. Rev.* **2018**, *47*, 2431−2453.
(16) Gupta, S. K.; Murugavel, R. Enriching lanthanide single-ion magnetism through symmetry and axiality. *Chem. Commun.* **2018**, *54*, 3685−3696.
(17) Demir, S.; Gonzalez, M. I.; Darago, L. E.; Evans, W. J.; Long, J. R. Giant coercivity and high magnetic blocking temperatures for N_2^{3-} radical-bridged dilanthanide complexes upon ligand dissociation. *Nat. Commun.* **2017**, *8*, 2144.
(18) Gould, C. A.; McClain, K. R.; Reta, D.; Kragskow, J. G. C.; Marchiori, D. A.; Lachman, E.; Choi, E.-S.; Analytis, J. G.; Britt, R. D.; Chilton, N. F.; Harvey, B. G.; Long, J. R. Ultrahard magnetism from mixed-valence dilanthanide complexes with metal-metal bonding. *Science* **2022**, *375*, 198−202.
(19) Palii, A.; Tsukerblat, B.; Clemente-Juan, J. M.; Coronado, E. Magnetic exchange between metal ions with unquenched orbital angular momenta: basic concepts and relevance to molecular magnetism. *Int. Rev. Phys. Chem.* **2010**, *29*, 135−230.
(20) Mironov, V. S.; Chibotaru, L. F.; Ceulemans, A. Mechanism of a Strongly Anisotropic Mo^{III}-CN-Mn^{II} Spin-Spin Coupling in Molecular Magnets Based on the $[Mo(CN)_7]^{4-}$ Heptacyanometalate: A New Strategy for Single-Molecule Magnets with High Blocking Temperatures. *J. Am. Chem. Soc.* **2003**, *125*, 9750−9760.
(21) Singh, S. K.; Rajaraman, G. Can Anisotropic Exchange Be Reliably Calculated Using Density Functional Methods? A Case Study on Trinuclear Mn^{III}-M^{III}-Mn^{III} (M=Fe, Ru, and Os) Cyanometalate Single-Molecule Magnets. *Chem. − Eur. J.* **2014**, *20*, 113−123.
(22) Mironov, V. S. Strong exchange anisotropy in orbitally degenerate complexes. A new possibility for designing single-molecule magnets with high blocking temperatures. *J. Magn. Magn. Mater.* **2004**, *272-276*, e731−e733.
(23) Meng, X.; Shi, W.; Cheng, P. Magnetism in one-dimensional metal-nitronyl nitroxide radical system. *Coord. Chem. Rev.* **2019**, *378*, 134−150.
(24) Demir, S.; Jeon, I.-R.; Long, J. R.; Harris, T. D. Radical ligand-containing single-molecule magnets. *Coord. Chem. Rev.* **2015**, *289-290*, 149−176.
(25) Caneschi, A.; Gatteschi, D.; Sessoli, R.; Rey, P. Toward molecular magnets: the metal-radical approach. *Acc. Chem. Res.* **1989**, *22*, 392−398.
(26) Vaz, M. G. F.; Andruh, M. Molecule-based magnetic materials constructed from paramagnetic organic ligands and two different metal ions. *Coord. Chem. Rev.* **2021**, *427*, No. 213611.
(27) Inoue, K. Metal-aminoxyl-Based Molecular Magnets. *Struct. Bonding* **2001**, *100*, 61−91.
(28) Kanetomo, T.; Ishida, T. Strongest exchange coupling in gadolinium(III) and nitroxide coordination compounds. *Inorg. Chem.* **2014**, *53*, 10794−10796.
(29) Baker, M. L.; Blundell, S. J.; Domingo, N.; Hill, S.; Spectroscopy Methods for Molecular Nanomagnets. In: Gao, S. (eds) *Molecular Nanomagnets and Related Phenomena. Struct. Bond.*, 2014, *164*, 231−292. Springer, Berlin, Heidelberg. DOI: 10.1007/430_2014_155.
(30) Fedin, M. V.; Veber, S. L.; Gromov, I. A.; Ovcharenko, V. I.; Sagdeev, R. Z.; Bagryanskaya, E. G. Electron Spin Exchange Processes in Strongly Coupled Spin Triads. *J. Phys. Chem. A* **2007**, *111*, 4449−4455.
(31) Fedin, M. V.; Veber, S. L.; Bagryanskaya, E. G.; Ovcharenko, V. I. Electron paramagnetic resonance of switchable copper-nitroxide-based molecular magnets: An indispensable tool for intriguing systems. *Coord. Chem. Rev.* **2015**, *289-290*, 341−356.
(32) Allão, R. A.; Jordão, A. K.; Resende, J. A. L. C.; Cunha, A. C.; Ferreira, V. F.; Novak, M. A.; Sangregorio, C.; Sorace, L.; Vaz, M. G. F. Determination of the relevant magnetic interactions in low-dimensional molecular materials: the fundamental role of single crystal high frequency EPR. *Dalton Trans.* **2011**, *40*, 10843−10850.
(33) Cotton, F. A.; Holm, R. H. Magnetic investigations of spin-free cobaltous complexes III. On the existence of planar complexes. *J. Am. Chem. Soc.* **1960**, *82*, 2979−2983.
(34) de Souza, M. S.; Briganti, M.; Reis, S. G.; Stinghen, D.; Bortolot, C. S.; Cassaro, R. A. A.; Guedes, G. P.; da Silva, F. C.; Ferreira, V. F.; Novak, M. A.; Soriano, S.; Totti, F.; Vaz, M. G. F. Magnetic cationic copper(II) chains and a mononuclear cobalt(II) complex containing $[Ln(hfac)_4]^-$ blocks as couterions. *Inorg. Chem.* **2019**, *58*, 1976−1987.
(35) Tsukahara, Y.; Iino, A.; Yoshida, T.; Suzuki, T.; Kaizaki, S. Synthesis, magnetic properties, and electronic spectra of mixed ligand bis(β-diketonato)chromium(III) complexes with a chelated nitronyl nitroxide radical: X-ray structure of $[Cr(dpm)_2(NIT2py)]PF_6$. *J. Chem. Soc., Dalton Trans.* **2002**, 181−187.
(36) *Bruker*; v2014.5−0 ed.; Bruker AXS, Inc.: Madison, WI, USA., 2007.
(37) *Bruker*; v8.34A ed.; Bruker AXS, Inc.: Madison, WI, USA, 2013.
(38) Sheldrick, G. M. *SADABS*; University of Göttingen; Göttingen: Germany,1996.
(39) Sheldrick, G. M. A short history of SHELX. *Acta Crystallogr. A* **2008**, *A64*, 112−122.
(40) Macrae, C. F.; Edgington, P. R.; McCabe, P.; Pidcock, E.; Shields, G. P.; Taylor, R.; Towler, M.; Van de Streek, J. Mercury: visualization and analysis of crystal structures. *J. Appl. Crystallogr.* **2006**, *39*, 453−457.
(41) Bain, G. A.; Berry, J. F. Diamagnetic corrections and Pascal's constants. *J. Chem. Educ.* **2008**, *85*, 532.
(42) Hassan, A. K.; Pardi, L. A.; Krzystek, J.; Sienkiewicz, A.; Goy, P.; Rohrer, M.; Brunel, L.-C. Ultrawide band multifrequency high-field EMR technique: a methodology for increasing spectroscopic information. *J. Magn. Reson.* **2000**, *142*, 300−312.
(43) Guedes, G. P.; Zorzanelli, R. G.; Comerlato, N. M.; Speziali, N. L.; Santos-Jr, S.; Vaz, M. G. F. Two copper(II)-nitronyl nitroxide radical dimers with a bulky β-diketonate: synthesis, structure and magnetic behavior. *Inorg. Chem. Commun.* **2012**, *23*, 59−62.
(44) Matsuoka, N.; Yoshioka, N. Electronic structures and magnetic properties of copper(II) complexes with axially coordinated nitronyl nitroxide radicals. *Polyhedron* **2009**, *28*, 1875.
(45) Fegy, K.; Luneau, D.; Ohm, T.; Paulsen, C.; Rey, P. Two-Dimensional Nitroxide-Based Molecular Magnetic Materials. *Angew.-Chem., Int. Ed.* **1998**, *37*, 1270−1273.
(46) Tretyakov, E. V.; Koreneva, O. V.; Romanenko, G. V.; Shvedenkov, Y. G.; Ovcharenko, V. I. Synthesis, structure and magnetism of $M(hfac)_2$ complexes with spin labelled amides. *Polyhedron* **2004**, *23*, 763−772.
(47) Zheludev, A.; Barone, V.; Bonnet, M.; Delley, B.; Grand, A.; Ressouche, E.; Rey, P.; Subra, R.; Schweizer, J. Spin density in a nitronyl nitroxide free radical. Polarized neutron diffraction investigation and ab initio calculations. *J. Am. Chem. Soc.* **1994**, *116*, 2019−2027.
(48) Chilton, N. F.; Anderson, R. P.; Turner, L. D.; Soncini, A.; Murray, K. S. PHI: a powerful new program for the analysis of

anisotropic monomeric and exchange-coupled polynuclear *d*- and *f*-block complexes. *J. Comput. Chem.* **2013**, *34*, 1164−1175.
(49) Wang, C.; Ma, Y.; Wang, Y.; Wang, Q.; Li, L.; Cheng, P.; Liao, D. A new quinoxalinyl-substituted nitronyl nitroxide radical and its five-spin Cu^{II} and four-spin Mn^{II} complexes: syntheses, crystal structures, and magnetic properties. *Aust. J. Chem.* **2012**, *65*, 672−679.
(50) Yang, M.; Xie, S.; Liang, X.; Zhang, Y.; Dong, W. A novel functional nitronyl nitroxide and its manganese and cobalt complexes: synthesis, structures and magnetic properties. *Polyhedron* **2019**, *161*, 132−136.
(51) Bhatt, P.; Kolanji, K.; Ivanova, A.; Yogi, A.; Jakob, G.; Mukadam, M. D.; Yusuf, S. M.; Baumgarten, M. Magnetic exchange interaction in nitronyl nitroxide radical-based single crystals of 3d metal complexes: a combined experimental and theoretical study. *ACS Omega* **2018**, *3*, 2918−2933.
(52) Li, T.; Shi, X. J.; Chen, P. Y.; Yu, S. J.; Tian, L. A series bi-spin transition metal(II) complexes based on triazole nitronyl nitroxide radical. *Inorg. Chim. Acta* **2017**, *461*, 206−212.
(53) Kalizs, M.; Novak, M. A.; Pinheiro, C. B.; Florencio, A. S.; Chapuis, G.; Caneschi, A.; Vaz, M. G. F. Synthesis, structural and magnetic characterization of a new copper(II)-nitronyl nitroxide radical complex. *J. Braz. Chem. Soc.* **2007**, *18*, 916−923.
(54) Luneau, D.; Romero, F. M.; Ziessel, R. Nitronyl Nitroxide Biradicals as Tetradentate Chelates: Unusually Large Metal-Nitroxide Ferromagnetic Interactions. *Inorg. Chem.* **1998**, *37*, 5078−5087.
(55) Caneschi, A.; Gatteschi, D.; Lalioti, N.; Sessoli, R.; Sorace, L.; Tangoulis, V.; Vindigni, A. Ising-Type Magnetic Anisotropy in a Cobalt(II) Nitronyl Nitroxide Compound: A Key to Understanding the Formation of Molecular Magnetic Nanowires. *Chem. − Eur. J.* **2002**, *8*, 286−292.
(56) Stoll, S.; Schweiger, A. EasySpin, a Comprehensive Software Package for Spectral Simulation and Analysis in EPR. *J. Magn. Reson.* **2006**, *178*, 42−55.
(57) Hill, S.; Datta, S.; Liu, J.; Inglis, R.; Milios, C. J.; Feng, P. L.; Henderson, J. J.; del Barco, E.; Brechin, E. K.; Hendrickson, D. N. Magnetic quantum tunneling: insights from simple molecule-based magnets. *Dalton Trans.* **2010**, *39*, 4693−4707.
(58) Zhang, Y.; Malik, U. P.; Quiggins, B.; Nguyen, H.; Beedle, C. C.; Kovalev, A. E.; Clérac, R.; Hill, S.; Bythell, B. J.; Holmes, S. M. Structure-property relationships in tricyanoferrate(III) building blocks and trinuclear cyanide-bridged complexes. *Eur. J. Inorg. Chem.* **2016**, *2016*, 2432−2442.
(59) Gatteschi, D.; Sessoli, R.; Villain, J. *Molecular Nanomagnets*; Oxford University Press: Oxford, 2006; DOI: 10.1093/acprof:oso/9780198567530.001.0001.
(60) Feng, X.; Liu, J.; Harris, T. D.; Hill, S.; Long, J. R. Slow magnetic relaxation induced by a large transverse zero-field splitting in a $Mn^{II}Re^{IV}(CN)_2$ single-chain magnet. *J. Am. Chem. Soc.* **2012**, *134*, 7521−7529.
(61) Nguyen, T. N.; Shiddiq, M.; Ghosh, T.; Abboud, K. A.; Hill, S.; Christou, G. Covalently Linked Dimer of Mn_3 Single-Molecule Magnets and Retention of Its Structure and Quantum Properties in Solution. *J. Am. Chem. Soc.* **2015**, *137*, 7160−7168.
(62) Zipse, D.; North, J. M.; Dalal, N. S.; Hill, S.; Edwards, R. S. Characterization of the S=9 excited state in Fe_8Br_8 by electron paramagnetic resonance. *Phys. Rev. B* **2003**, *68*, No. 184408.
(63) Hill, S.; Maccagnano, S.; Park, K.; Achey, R. M.; North, J. M.; Dalal, N. S. Detailed single-crystal EPR line shape measurements for the single-molecule magnets Fe_8Br and Mn_{12}-acetate. *Phys. Rev. B* **2002**, *65*, 22410.
(64) Barra, A. L.; Gatteschi, D.; Sessoli, R. High-frequency EPR spectra of $[Fe_8O_2(OH)_{12}(tacm)_6]Br_8$: a critical appraisal of the barrier for the reorientation of the magnetization in single-molecule magnets. *Chem. − Eur. J.* **2000**, *6*, 1608−1614.
(65) Winter, S. M.; Datta, S.; Hill, S.; Oakley, R. T. Magnetic anisotropy in a heavy atom radical ferromagnet. *J. Am. Chem. Soc.* **2011**, *133*, 8126−8129.
(66) Sebastian, S. E.; Tanedo, P.; Goddard, P. A.; Lee, S.-C.; Wilson, A.; Kim, S.; Cox, S.; McDonald, R. D.; Hill, S.; Harrison, N.; Batista, C. D.; Fisher, I. R. Role of anisotropy in the spin-dimer compound $BaCuSi_2O_6$. *Phys. Rev. B* **2006**, *74*, No. 180401.
(67) Marbey, J.; Gan, P.-R.; Yang, E.-C.; Hill, S. Magic-angle effects in a trigonal Mn^{III}_3 cluster: deconstruction of a single-molecule magnet. *Phys. Rev. B* **2018**, *98*, No. 144433.
(68) Prescimone, A.; Morien, C.; Allan, D.; Schlueter, J. A.; Tozer, S. W.; Manson, J. L.; Parsons, S.; Brechin, E. K.; Hill, S. Pressure-driven orbital reorientations and coordination-sphere reconstructions in $[CuF_2(H_2O)(pyz)]$. *Angew. Chem., Int. Ed.* **2012**, *51*, 7490−7494.
(69) del Barco, E.; Hill, S.; Beedle, C. C.; Hendrickson, D. N.; Tupitsyn, I. S.; Stamp, P. C. E. Tunneling and inversion symmetry in single-molecule magnets: the case of the Mn_{12} wheel molecule. *Phys. Rev. B* **2010**, *82*, No. 104426.
(70) Mironov, V. S. Origin of Dissimilar Single-Molecule Magnet Behavior of Three $Mn^{II}_2Mo^{III}$ Complexes Based on $[Mo^{III}(CN)_7]^{4-}$ Heptacyanomolybdate: Interplay of $Mo^{III}−CN−Mn^{II}$ Anisotropic Exchange Interactions. *Inorg. Chem.* **2015**, *54*, 11339−11355.
(71) Singh, S. K.; Rajaraman, G. Probing the origin of magnetic anisotropy in a dinuclear $\{Mn^{III}Cu^{II}\}$ single-molecule magnet: the role of exchange anisotropy. *Chem. − Eur. J.* **2014**, *20*, 5214−5218.
(72) Harris, T. D.; Coulon, C.; Clérac, R.; Long, J. R. Record ferromagnetic exchange through cyanide and elucidation of the magnetic phase diagram for a $Cu^{II}Re^{IV}(CN)_2$ chain compound. *J. Am. Chem. Soc.* **2011**, *133*, 123−130.
(73) Dei, A.; Gatteschi, D.; Pardi, L.; Barra, A. L.; Brunel, L. C. Millimeter band EPR spectra reveal large zero-field splittings in copper(II)-semiquinonato complexes. *Chem. Phys. Lett.* **1990**, *175*, 589−592.